**Proceedings of the ASME 2010 3rd Joint US-European Fluids Engineering Summer Meeting and
8th International Conference on Nanochannels, Microchannels, and Minichannels
FEDSM-ICNMM2010
August 1-5, 2010, Montreal, Canada**

PIV MEASUREMENTS OF TURBULENT FLOW IN A CHANNEL WITH SOLID OR PERFORATED RIBS

Lei Wang[*]
Heat Transfer Division
Lund University
SE-22100 Lund, Sweden
Email: lei.wang@energy.lth.se

Mirko Salewski
Risø National Laboratory
for Sustainable Energy,
Technical University of Denmark,
DK-4000 Roskilde, Denmark

Bengt Sundén
Heat Transfer Division
Lund University
SE-22100 Lund, Sweden

ABSTRACT

Particle image velocimetry measurements are performed in a channel with periodic ribs on one wall. We investigate the flow around two different rib configurations: solid and perforated ribs with a slit. The ribs obstruct the channel by 20% of its height and are arranged 10 rib heights apart. For the perforated ribs, the slit height is 20% of the rib height, and the open-area ratio is 16%. We discuss the flow in terms of mean velocity, streamlines, vorticity, turbulence intensity, and Reynolds shear stress. We find that the recirculation bubbles after the perforated ribs are significantly smaller than those after the solid ribs. The reattachment length after perforated ribs is smaller by about 45% compared with the solid ribs. In addition, the Reynolds shear stresses around the perforated ribs are significantly smaller than in the solid rib case, leading to a reduction of the pressure loss in the perforated rib case.

INTRODUCTION

Channels roughened with periodic ribs are widely applied in various cooling passages, e.g. in gas turbine blades. Periodic ribs increase the thermal performance of the cooling passage compared with smooth walls. However, ribs also increase the pressure loss of the flow through the channel. One seeks to design channels with simultaneously high heat transfer rates and a low pressure loss. Solid ribs with rectangular shape have the advantage that they are easy manufacture. The geometry of

the arrangement of such solid rectangular ribs is a possible passive control parameter. Many experimental and computational studies have characterized the flow field in such ribbed channels [1–8]. The flow separates from the rear edge of each rib, forming a highly unsteady free shear layer. A recirculation bubble forms behind the rib, and the mean flow reattaches to the wall after the separation bubble usually before the next rib. The heat transfer rates attain a maximum near the time-mean reattachment line [9]. However, the heat transfer coefficients decrease sharply in the region of a small secondary eddy in the corner immediately downstream of the rib, and a hot spot emerges in this region. In order to eliminate this hot spot, past efforts were focussed on the shape of the rib. Various different types of ribs have been shown to improve the thermal performance compared with rectangular ribs. For example, it has been possible to reduce the hot spot with triangular, trapezoidal, semicircular, or sinusoidal rib shapes [10–15]. Also various types of perforation in the ribs have been investigated, and this is also the subject of the present work. Hwang and Liou [16] found that perforated ribs can effectively suppress the formation of hot spots since part of the air flow passes through the perforated ribs and directly impinges on the recirculating region behind the rib. Buchlin [17] implemented infrared thermography to investigate the heat transfer characteristics in a channel equipped with different perforated ribs. He likewise found that there was no hot spot in the case of perforated ribs. In addition, he also found that the perforated ribs with chevron-clearance produce the highest heat transfer rates. More recently, Panigrahi et al. [18, 19] carried out particle image

---

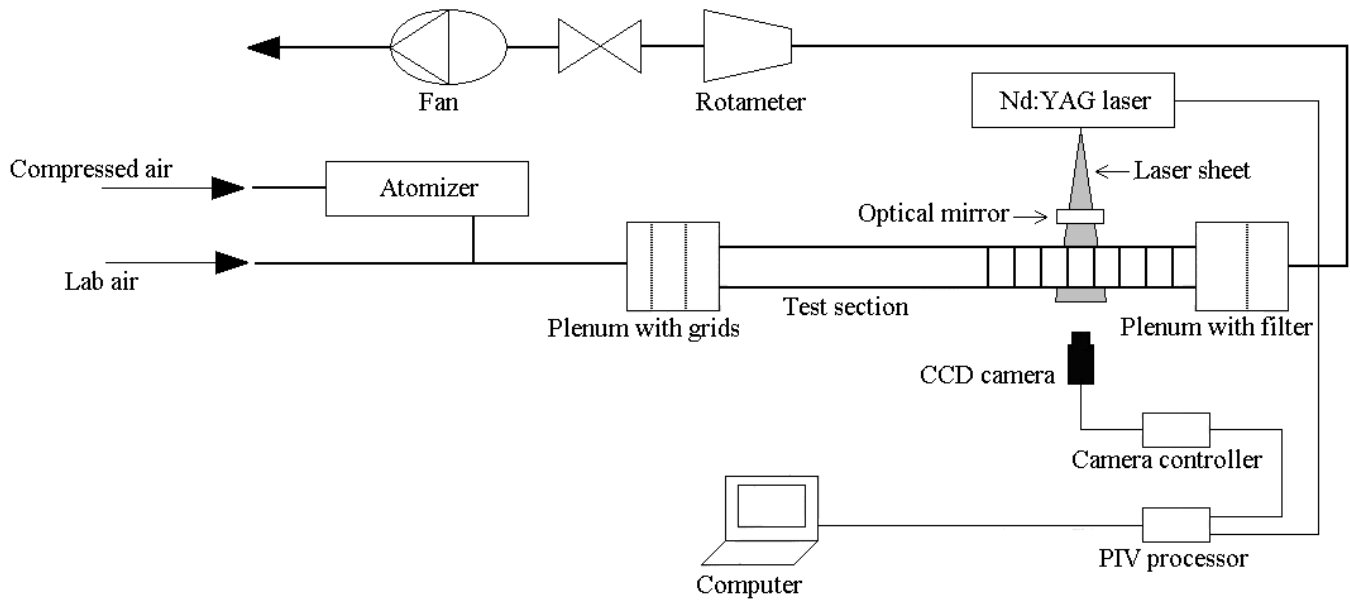[*]Address all correspondence to this author.

FIGURE 1.   SKETCH OF EXPERIMENTAL SETUP

velocimetry (PIV) measurements in a channel fitted with perforated ribs of various shapes. They found that the generation of longitudinal and transverse vortical structures and their interaction are responsible for higher mixing and heat transfer rates. Simultaneously, the pressure penalty was reduced for perforated rib geometries. These results have also been computed [20]. However, Kukreja and Lau [21] obtained results that were apparently at variance. They conducted transient liquid crystal thermography experiments to measure the local heat transfer for turbulent flows through a square channel with ribs of various configurations, including perforated ribs, on two opposite walls. The rib height-to-hydraulic diameter ratio and the rib pitch-to-height ratio were 0.125 and 10, respectively, and the Reynolds number ranged from 15,000 to 50,000. Perforated ribs were found to be not as good as solid ribs in enhancing heat transfer. Even though perforated ribs produced the lower pressure drop, they did not improve thermal performance. Increasing the size of the holes, the number of holes, or the total hole area did not enhance the overall heat transfer.

In the present study, the flow fields in a channel equipped with solid and perforated ribs are examined, and a detailed comparison between them is presented. This work extends our previous investigations which were focussed on solid ribs [6–8]. A two-dimensional particle image velocimetry (PIV) is used to measure the instantaneous velocity fields. Specific interest has been focused on the mean velocity, streamlines, vorticity, and turbulence properties. With aid of Reynolds decomposition, distinct vortical structures behind the solid and perforated ribs are

clearly identified. We add some focus on the role of the jet emanating into the region downstream of the rib where it encounters a crossflow due to recirculation bubble. This work is expected to provide guidance in the design of perforated rib geometries by showing the advantages compared with the simpler solid ribs.

EXPERIMENTAL PROCEDURES
Channel geometry
The experimental setup is sketched in Fig. 1. Air with ambient temperature is sucked into the channel by a fan. The test section consists of a 1500 mm long channel with a cross section of 50 mm × 50 mm. The first half of the channel is smooth, and the second half of the channel is roughened with ribs. Only one wall is fitted with periodic transverse ribs. The height of ribs is 10 mm which obstructs the channel by 20% of its height. The rib pitch, defined as the distance from one leading edge to the next leading edge, is 10 rib heights, as illustrated in the top of Fig. 2. The geometry of perforated ribs is seen in the bottom of Fig. 2. The slit has a size of is 40 mm × 2 mm, and the open-area ratio, defined as the ratio of the area of the slit and the area of the entire rib (including the slit), is 16%. The rib height is represented by e, the rib pitch by P, and the channel height is denoted by H. The Cartesian coordinates x, y, and z are defined in such a way that the x-axis is in the streamwise direction, the y-axis is the wall-normal direction, and z-axis is the spanwise direction. The time-mean components of the velocity in the x- and y-directions are denoted by U, and V, respectively, and the
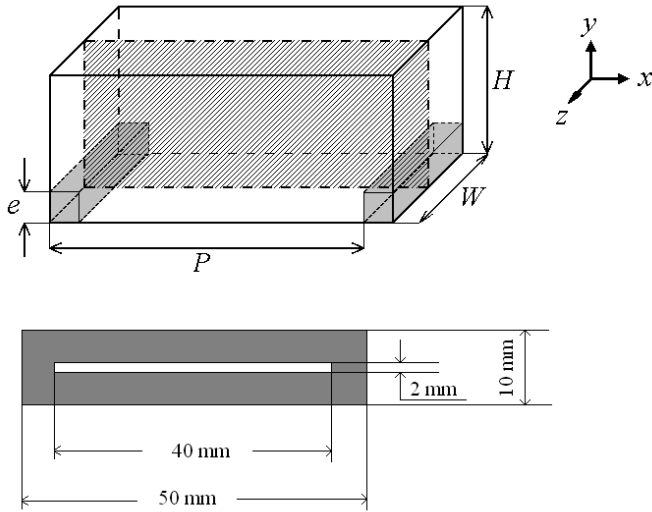
2

FIGURE 2. TOP: RIB CONFIGURATION IN THE CHANNEL; BOTTOM: FRONT VIEW OF THE PERFORATED RIB

(a) SOLID RIB

(b) PERFORATED RIB

FIGURE 3. SIDE VIEW OF MEAN STREAMLINES IN THE MID-SPAN PLANE

corresponding fluctuating components are denoted by u' and v'. The Reynolds number is $22,000$ based on the bulk-mean velocity $U_0 = 6.7$ m/s and the channel height H. In the present study, the flow around the seventh rib is investigated. This position is located at $X/D_h = 28$, where X is the distance of the seventh rib from the inlet, and D_h is the hydraulic diameter of the channel. Throughout this paper, all quantities are normalized by the characteristic scales for length and velocity e and U_0, respectively.

Particle Image Velocimetry System

A commercially available PIV system developed by Dantec Dynamics is used in the present investigation. An oil-based aerosol is generated by a TSI 9306 six-jet atomizer. In order to get a homogeneous distribution of seeding particles, a plenum with two grids is connected to the channel inlet. The mean particle diameter is about 1 μm and the concentration is regulated by the compressed air pressure and the number of Laskin nozzles. A Quantel Q-switched Nd:YAG laser provides pulsed illuminations with a wavelength of 532 nm. The duration of each pulse is 10 ns, and the maximum output energy is 120 mJ. The light-sheet thickness in the test section is kept at 0.8 mm. A digital camera containing a CCD chip with 1280×1024 pixels and a Nikon AF Micro 60f/2.8D lens with an optical filter are used to record the particle images. The size of the interrogation window is 32×32 pixels with 50% overlapping. This gives a spatial resolution $\delta/e = 0.067$ (δ is the spacing between vectors). The time interval between laser pulses is set such that the particles move at most 8 pixels between the pair of images. In the present study, the time interval is 10 μs which gives the optimum measurement
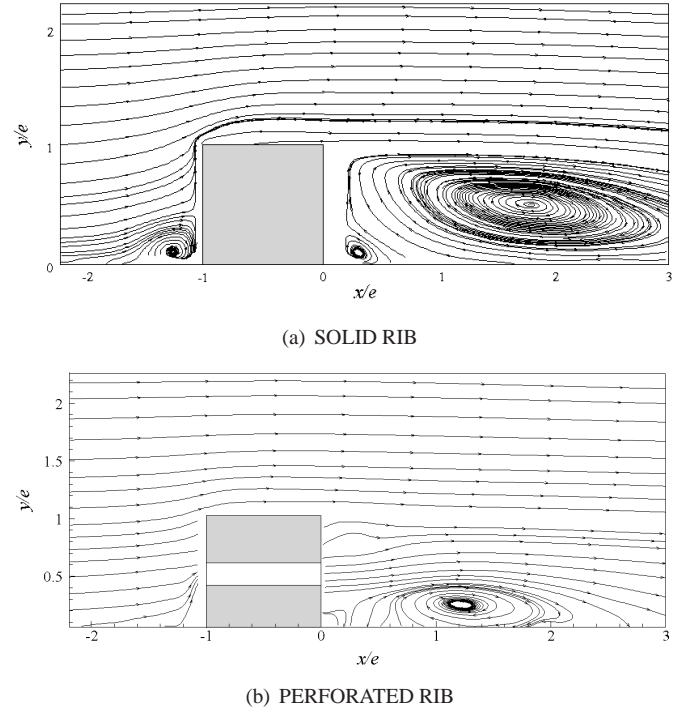
of the velocity. Within each window, the number of seeding particles is greater than 5 and the particle image size projected onto the CCD sensor is approximately 3 pixels. FlowMap software is used for the data processing. FFT-based cross-correlation in conjunction with a two-dimensional Gaussian fit is applied to find the correlation peak position. When the instantaneous velocity field is calculated, a peak-height validation and a moving-average validation are applied to the raw maps to detect outliers and replace them by vectors estimated from surrounding values. To minimize the noise, a top hat filter with uniform weighting is implemented. The averaging area of the filter is 3×3 pixels. Assuming that the measured particle displacement is accurate to 0.1 pixels, the error is less than 2% for the displacement of 8 pixels. An ensemble of 1000 instantaneous velocity samples is generated with an acquisition rate of 4 Hz. It is found that the turbulent shear stresses converge well as the number of samples is greater than 700 (deviation is less than 3%). Another error affecting the Reynolds shear stress is the spatial resolution of PIV. In the present experiment, the uncertainty for the shear stress is estimated to be about 10%, which takes into account the number of samples and PIV spatial resolution.

3
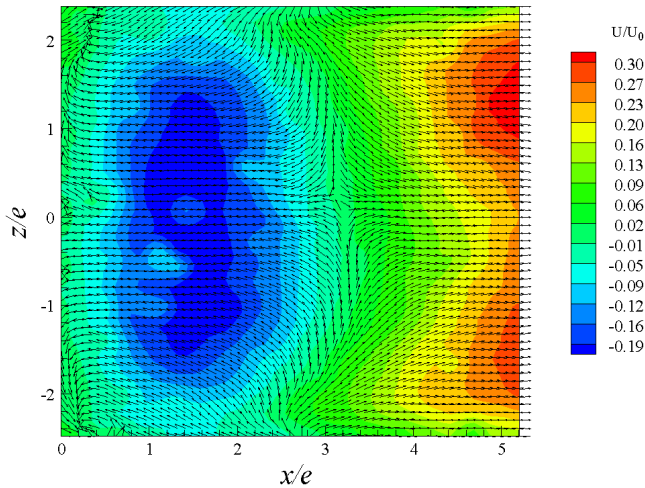
(a) SOLID RIB
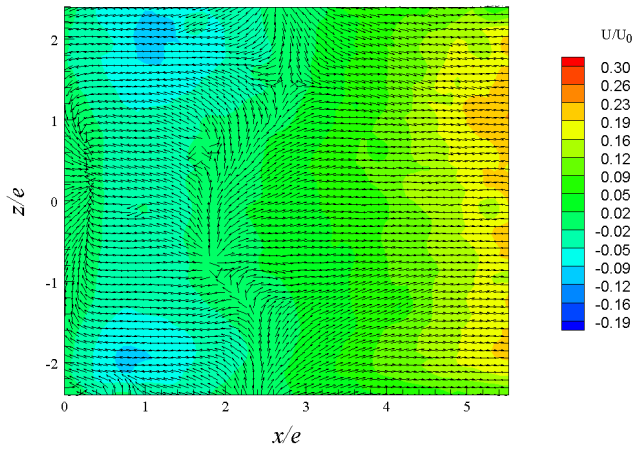
(b) PERFORATED RIB

FIGURE 4. TOP VIEW OF THE MEAN VELOCITY FIELD JUST ABOVE THE WALL

RESULTS
Comparison of the Recirculation Zones and Reattachment Points for Solid and Perforated Ribs

First we focus on the recirculation bubble and the reattachment of the flow to the wall and compare these salient flow features for the two types of rib geometries. Figures 3(a) and 3(b) show the mean streamlines past the solid and perforated rib in the mid-span plane, respectively. For the solid ribs, three zones of recirculating fluid are found in the vicinity of each rib which are pictured in Fig. 3(a). The flow is dominated by a large recirculation bubble behind the rib which extends from very close to the rib ($x/e < 0.2$) to several rib lengths ($x/e > 3$). A secondary vortex forms between the large recirculation bubble and the lee-
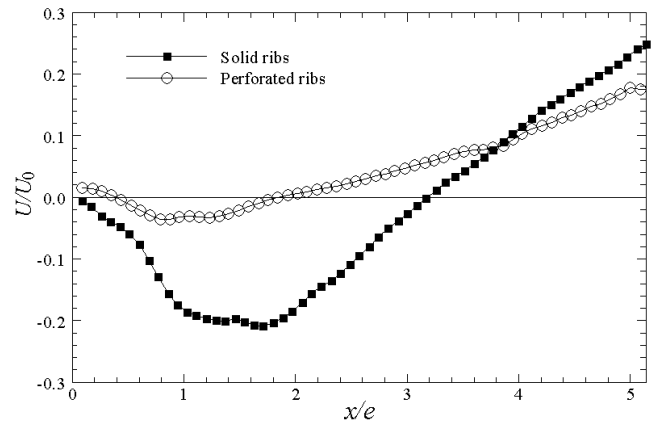

FIGURE 5. STREAMWISE VELOCITY ALONG THE CENTERLINE IN THE PLANE JUST ABOVE THE WALL

ward corner of the rib. The presence of this secondary vortex is correlated with the hot spot mentioned in the introduction. Additionally, a small separation bubble forms upstream of the rib due to the adverse pressure gradient which the flow approaching the rib encounters. The slit in the rib changes the flow patterns significantly as is evident in Fig. 3(b). The pressure downstream of the rib is smaller than upstream of the rib, and this pressure difference drives a flow through the slit. This flow emerges on the leeward side of the rib as a jet. Thus streamwise momentum is injected into the region behind the rib. We may note that the jet is deflected towards the center of the channel because the rotation sense of the recirculation bubble creates a crossflow towards the channel center. The slit is oriented transverse to this crossflow, i.e. the cross-stream direction of the slit is wider than the streamwise direction with respect to the crossflow. Jets emanating from such nozzle geometries are known to be efficient mixers [22]. The fluid emanating from the slit as a jet is therefore expected to mix efficiently with the recirculating fluid in the region downstream of the rib. Thereby streamwise momentum (with respect to the channel flow) is added to the recirculation region. The recirculation bubble is significantly smaller in the case of a perforated rib compared with the solid rib case, and it does not extend as far towards the rib ($x/e > 0.5$) or downstream ($x/e < 2.5$). Moreover, we do not observe the secondary vortex in the leeward corner between the rib and the wall as the size of this corner eddy is below the spatial resolution in Fig. 3. Similarly, we find no separation bubble in the upstream region of the perforated rib. The adverse pressure gradient upstream of the perforated rib is smaller compared with the solid rib case since flow can pass through the slit.

Figure 4 plots the mean flow fields in the $x - z$ plane (the top view) just above the wall for solid and perforated rib cases. It should be mentioned that the exact wall-unit value of this plane

4

is difficult to estimate because the laser sheet thickness itself is 0.8 mm. In this figure, the spanwise reverse flow for both cases is clearly discernible. It is also apparent that the flow over the ribs is three-dimensional in nature and that also the three-dimensional pattern is different for the solid rib case and the perforated rib case. In the case of the solid ribs, the reattachment length as a function of z/e is largest in the center of the channel for $z/e \approx 0$. The reattachment point can be regarded as the position where the streamwise velocity becomes zero. Thus the footprint of the recirculation bubble in Figure 4(a), i.e. the locus of points with zero streamwise velocities, has a convex shape. Such a convex shape forms due to the effect of the side walls on both sides. Contrarily, in the case with the slit in the rib in Figure 4(b), the streamwise momentum entering the region behind the rib through the slit gives the footprint a concave shape: the reattachment length is smaller for $z/e \approx 0$ compared with the larger values of $|z/e| > 1$. It should be kept in mind here that the slit does not cover the entire width of the rib, and this will contribute to a concave shape in Figure 4(b).

Figure 5 displays the streamwise velocity along the centerline in this plane. As mentioned before, the position where the streamwise velocity becomes zero can be regarded as the reattachment point. For the solid rib the reattachment length is 3.2 e whereas for the perforated rib the reattachment length is reduced to 1.8 e at the center of the channel. The smaller reattachment length in the perforated rib case is also consistent with the smaller recirculation bubble which is in agreement with the result in Fig. 3. In addition, Fig. 5 shows that the magnitude of the maximum negative velocity associated with the reverse flow is considerably smaller in the case with perforated ribs by almost an order of magnitude.

Profiles of Mean Velocity, Root Mean Square, and Reynolds Shear Stresses

In this section we discuss profiles of the mean velocities in streamwise and wall-normal directions, their root mean squares, and the Reynolds shear stresses and compare the solid rib with the perforated rib in these parameters. In Figure 6(a) profiles of the mean streamwise velocity component are plotted at different streamwise locations in the mid-span plane for the solid rib. The flow velocity is increased above the rib due to continuity. The flow separates at the leeward corner of the rib, and an unsteady shear layer is formed. Below the shear layer, a large recirculation zone is formed: the reverse flow is demonstrated in the region behind the rib ($x/e > 1$). In the case of the perforated rib in Fig. 6(b), the velocity profiles just behind the rib attain a qualitatively different shape. At $x/e = 0.5$, a local peak can be observed at $y/e \approx 0.7$ in the velocity profile for the perforated rib as a consequence of the jet flow passing through the slit. This jet flow injects streamwise momentum into the near-wall region behind the rib and prevents the formation of a large recircula-
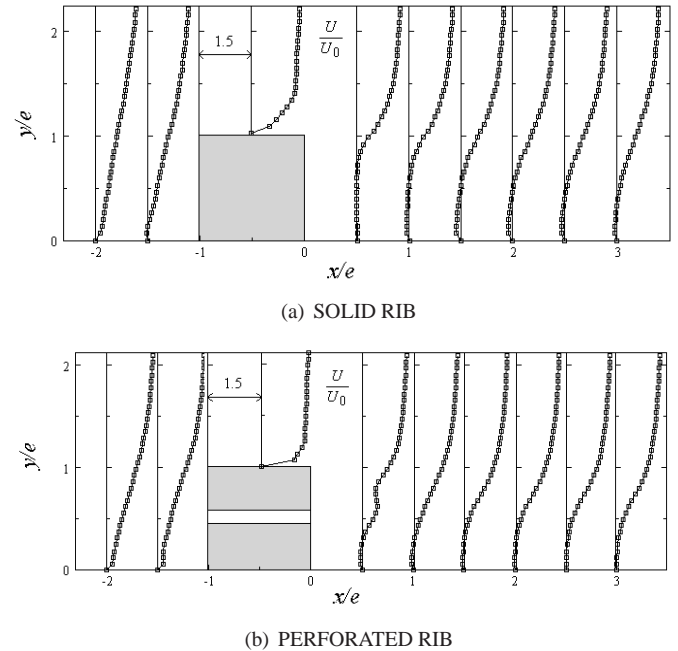

(a) SOLID RIB

(b) PERFORATED RIB

FIGURE 6. MEAN STREAMWISE VELOCITY PROFILES AT VARIOUS LOCATIONS IN THE MID-SPAN PLANE

tion zone. As noted before the jet is deflected upwards in the crossflow due to recirculation bubble in the near wall region: the local peak in the velocity profile is above the slit (which is at $y/e \approx 0.5$). This extra momentum at regions above $y/e \approx 0.75$ flattens the velocity gradients for the perforated ribs compared with the solid ribs. Therefore less turbulence is generated in the shear layer for the perforated ribs as we will find when we discuss the root mean square quantities below. Additionally, the extra momentum moves the inflection point in the velocity profile downwards. For the solid rib, the position of the inflectional point is about $y/e \approx 1$. However, this position is closer to the wall and corresponds to $y/e \approx 0.75$ for the perforated rib. The flow above the rib is not changed significantly because only a tiny fraction of the flow passes through the slit.

Figure 7(a) shows the mean wall-normal velocity component at different streamwise locations in the mid-span plane for the solid rib. The maximum wall-normal velocity component is upward directed and found just ahead of the rib where the portion of the flow blocked by the rib forces upwards. Behind the rib, the flow is downward directed into the low pressure region behind the rib, except for the region where the recirculation bubble dictates an upward flow close to the rib in the region given by $x/e < 1.5$ and $y/e < 1$. The magnitude of the upward velocity just ahead of the rib is smaller for the perforated rib as can be seen in Figure 7(b). Part of the flow passes through the slit of the rib. The jet in crossflow just after the rib increases the height of positive peak in the wall-normal velocities ($x/e = 0.5$) signif-
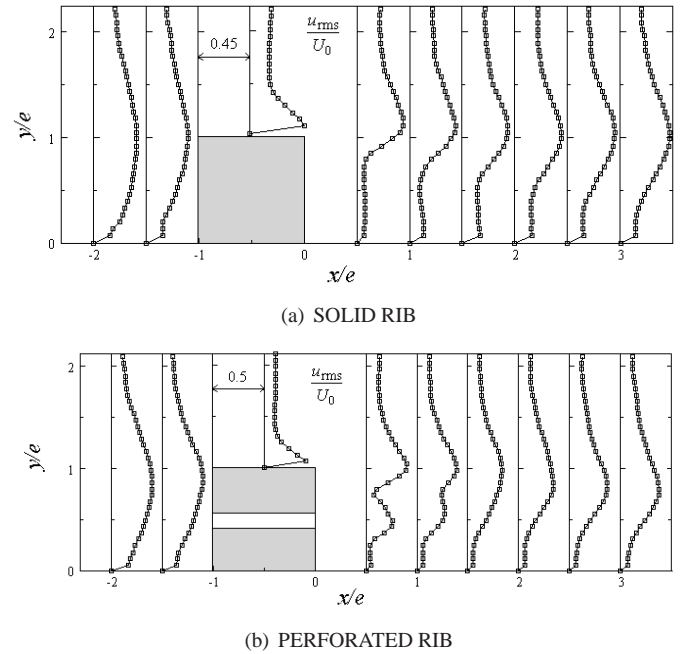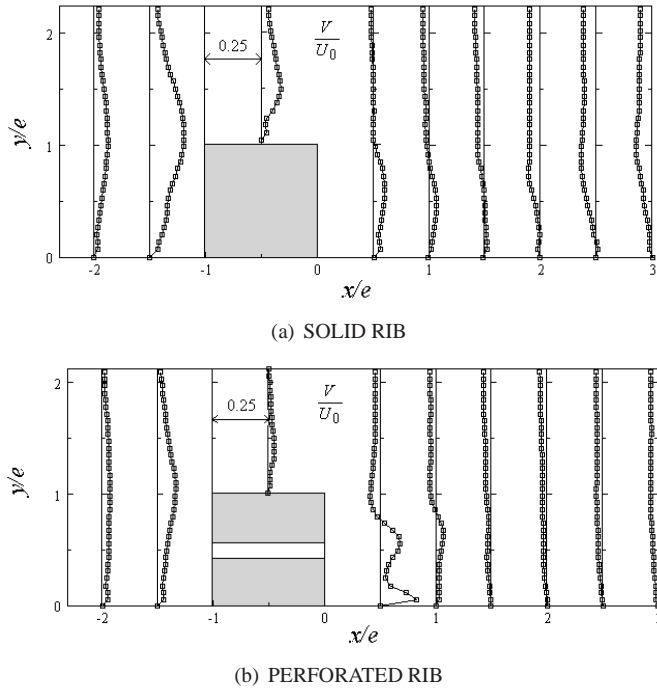
(a) SOLID RIB

(b) PERFORATED RIB

FIGURE 7. MEAN WALL-NORMAL VELOCITY PROFILES AT VARIOUS LOCATIONS IN THE MID-SPAN PLANE

(a) SOLID RIB

(b) PERFORATED RIB

FIGURE 8. PROFILES OF u_{rms} AT VARIOUS LOCATIONS IN THE MID-SPAN PLANE

(a) SOLID RIB

(b) PERFORATED RIB

FIGURE 9. PROFILES OF v_{rms} AT VARIOUS LOCATIONS IN THE MID-SPAN PLANE

icantly as the jet has deflected in the upward direction. Thereby also the velocity gradients are increased. Additionally, there is a stronger negative peak at $x/e = 1$ and $y/e \approx 1$ compared with the solid rib case showing an enhanced flow of downward moving fluid just after the rib for perforated ribs compared with solid ribs.

Figure 8 presents the profiles of the root mean square streamwise velocity u_{rms} at different streamwise locations. For the solid rib in Figure 8(a), the position where u_{rms} attains a maximum value is around $y/e \approx 1$. This position can be interpreted as the center of the shear layer because it coincides with the inflectional point in the mean streamwise velocity profile shown in Fig. 6. In addition, a large value of u_{rms} is found at the rib top which is well in agreement with the simulated results by Cui et al. [23]. For the perforated rib in Figure 8(b), two peaks are observed in the u_{rms} profiles just behind the rib ($x/e < 1$) at about $y/e \approx 1$ and $y/e \approx 0.5$. The additional peak is due to the turbulence generated by the deflecting jet just behind the rib. The maximum in u_{rms} is as expected below the deflecting jet which may be defined as the locus of maximum U. The shear layer below the deflecting jet has steeper velocity gradients than above the deflecting jet, and therefore the turbulence below the jet is more pronounced than above the jet. Further downstream, it is found that the position of the maximum value of u_{rms} approaches the wall and falls to $y/e \approx 0.75$, which coincides with the position of the inflectional point in the velocity profiles shown in
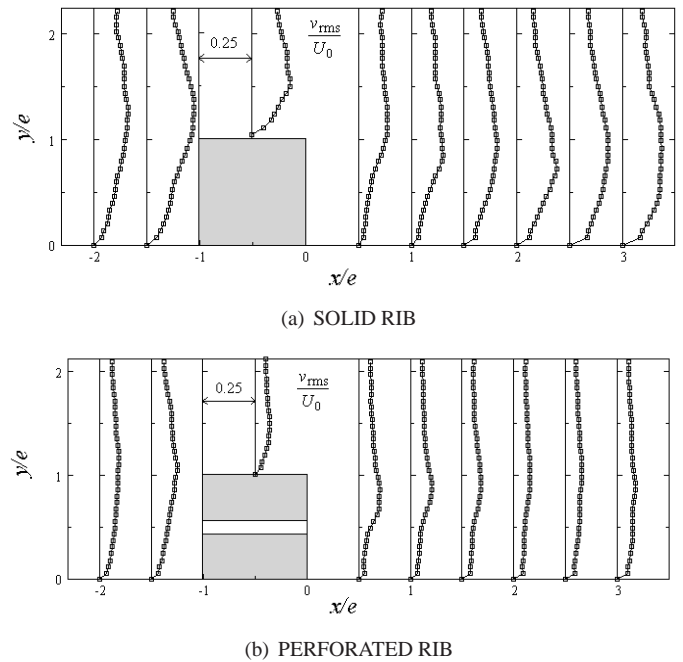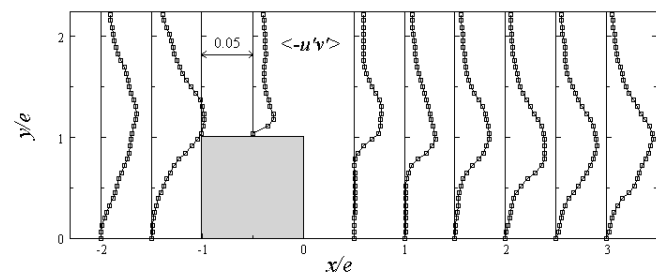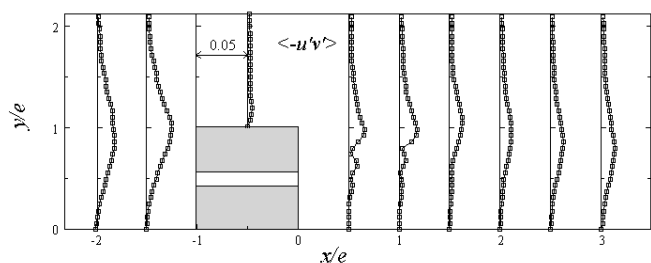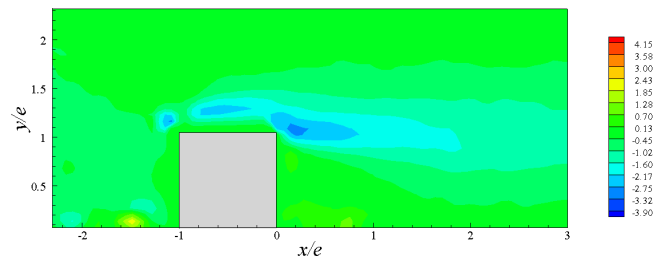
(a) SOLID RIB

(b) PERFORATED RIB

FIGURE 10. REYNOLDS SHEAR STRESS PROFILES AT VARIOUS LOCATIONS IN THE MID-SPAN PLANE, THE QUANTITIES ARE NORMALIZED BY $U_0{}^2$.

(a) SOLID RIB

(b) PERFORATED RIB

FIGURE 11. MEAN SPANWISE VORTICITY $\bar{\omega}_z$. THE QUANTITIES ARE NORMALIZED BY U_0/e.
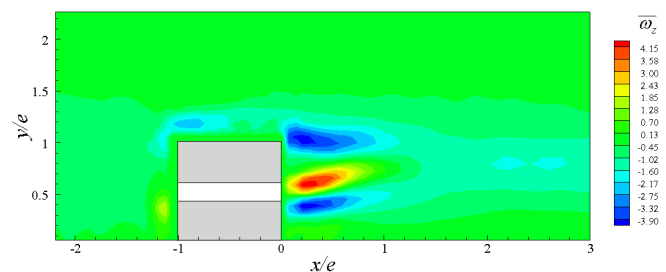
Fig. 6(b). One may note that the magnitudes of u_{rms} are lower in the case of the perforated ribs for corresponding positions, except for in the jet region directly behind the rib. The reason for this is that the velocity gradients in the shear layer are smaller for perforated ribs compared with solid ribs as we demonstrated in Fig. 6. Therefore less turbulence is generated.

Figure 9 shows the profiles of the v_{rms} at different locations. For the solid rib in Fig. 9(a), the largest value of v_{rms} is found just ahead of the rib where the mean channel flow encounters the upward forcing fluid. For the perforated rib in Fig. 9(b), the magnitude of v_{rms} at all the locations is smaller compared with the solid rib case. The exception is a small region on the leeward side of the rib where the jet generally increases the turbulence levels. Unlike the u_{rms}, the double-peak distribution is not seen in the v_{rms} profiles just behind the perforated rib in correspondence to the flow direction of the deflecting jet.

Figure 10 displays the profiles of the Reynolds shear stress at different locations. For the solid rib case in Fig. 10(a), it is clear that the maximum Reynolds shear stresses occur at the leading edge of the rib which is in good agreement with the results of Cui et al. [23]. The sign of the Reynolds shear stress at the leading edge is as expected. Fluid particles forcing upwards will have a tendency to have more momentum in the upwards direction than average ($v' > 0$) but less momentum than average in the streamwise direction ($u' < 0$). Contrarily, fluid particles coming with the main channel flow will tendentiously have excess streamwise

momentum ($u' > 0$) but deficit upward momentum ($v' < 0$). For both idealized classes of fluid particles the average product will be negative and the Reynolds shear stress therefore positive. In the separated shear layer, the general trend is that the peak values of Reynolds shear stress increase with increasing distance from the rib. For the perforated rib in Fig. 10(b), the striking feature is that the Reynolds shear stresses are significantly smaller at all the locations compared with the solid rib except for the tiny region of the deflecting jet. This agrees with the fact that the turbulence levels where observed to be lower at corresponding locations. In the region of the jet in crossflow, the Reynolds shear stresses are slightly higher for the perforated ribs compared with the corresponding position for the solid rib (which has of course no jet in crossflow to generate the shear here). This result can explain the fact that the pressure penalty is reduced in the perforated rib case.

Vortex Identification for Solid and Perforated Ribs

The average spanwise vorticity $\bar{\omega}_z$ for solid and perforated ribs are presented in Fig. 11(a) and Fig. 11(b), respectively. The quantities are normalized by U_0/e. For both cases, the location of the maximum vorticity is different from the location foci of the primary recirculation bubble in Fig. 3. The lack of correspondence between the foci of the average streamlines and vorticity is not surprising because the vorticity only gives an indication on how large the velocity gradients are in the small scales. For the solid rib in Fig. 11(a), the vorticity with negative sign is signifi-
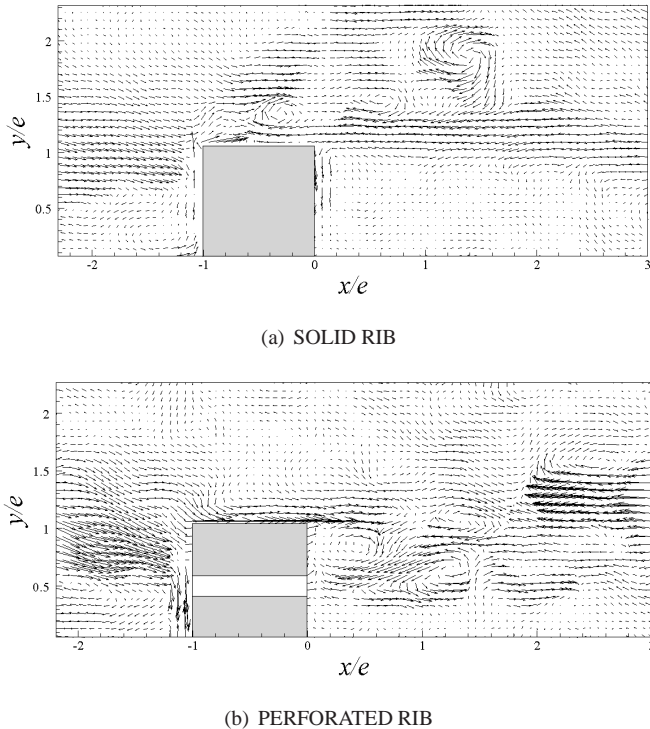
(a) SOLID RIB

(b) PERFORATED RIB

FIGURE 12. VORTEX IDENTIFICATION BY REYNOLDS DE-COMPOSITION

cant in the separated shear layer where the velocity gradient $\frac{\partial U}{\partial y}$ is dominant. For the perforated rib in Fig. 11(b), large values of the vorticity with alternating sign are observed just behind the rib in the shear layer of the deflecting jet.

Even though the isolated regions of significant vorticity give a clue of vortices in a velocity field, as mentioned above, vortices in vorticity are often overruled by regions of strong shear. In this case, if one wishes to understand the coherent structures in the flow, decomposition techniques are necessary to identify vortices. Reynolds decomposition into mean and fluctuating portions is one of the standard methods since it does a fair job of revealing the small-scale vortices [24]. The proper orthogonal decomposition is another option [7, 8, 22, 25]. In Fig. 12, one can visualize the vortices with aid of the Reynolds decomposition. For the solid rib in Fig. 12(a), three vortices which rotate in a clockwise sense are identified in an instantaneous flow field. They are entrained by the shear layer and shed downstream of the rib. The vortex furthest downstream has the clearest spiral pattern. On the contrary, for the perforated rib in Fig. 12(b), four vortices with different rotation manner are seen downstream of the rib. The vortices are formed in the region of the deflecting jet and are shed downstream. The vortex at $x/e \approx 1.2$ rotates in an anti-clockwise sense but the remaining vortices rotates in a clockwise direction. Changing sense of rotation for different vor-

tices is typical for this highly turbulent region. The most important difference here is the appearance of such vortical structure in the case of the perforated rib where a jet in crossflow emanates from the downstream face of the rib. These vortical structures increase mixing and heat and momentum transfer in the downstream region of the rib.

CONCLUSIONS

In this study, PIV measurements were performed in a channel equipped with solid and perforated ribs, respectively. Only one wall was fitted with periodic ribs. The ribs obstruct the channel by 20% of its height and are arranged 10 rib heights apart. The Reynolds number is 22,000 based on the bulk-mean velocity and channel height. The emphasis of this study was to investigate the flow structures in the vicinity of the rib. For the perforated rib, the important feature found is the smaller primary recirculation bubble downstream of the rib. Compared with the solid rib, the reattachment length was reduced by about 45%. The role of the jet flow passing through the slit of the rib is to add streamwise momentum to the recirculation bubble and to generate vortical structures. The fact that the jet is deflected by the crossflow increases the momentum transfer from the jet fluid to the recirculating fluid, the mixing, and the heat transfer. Lastly, we find that the Reynolds shear stresses are significantly smaller at almost all the streamwise locations for the perforated rib except for in the tiny region dominated by the deflecting jet. This fact is probably the reason for the reduction of the pressure penalty in this case.

ACKNOWLEDGMENT

REFERENCES

[1] Liou, T.-M., and Hwang, J.-J., 1992. "Turbulent heat transfer augmentation and friction in periodic fully developed channel flows". *Journal of Heat Transfer,* **114**(1), pp. 56–64.

[2] Rau, G., Çakan, M., Moeller, D., and Arts, T., 1998. "The effect of periodic ribs on the local aerodynamic and heat transfer performance of a straight cooling channel". *Journal of Turbomachinery,* **120**(2), pp. 368–375.

[3] Miyake, Y., Tsujimoto, K., and Nakaji, M., 2001. "Direct numerical simulation of rough-wall heat transfer in a turbulent channel flow". *International Journal of Heat and Fluid Flow,* **22**(3), pp. 237 – 244.

[4] Nagano, Y., Hattori, H., and Houra, T., 2004. "Dns of velocity and thermal fields in turbulent channel flow with transverse-rib roughness". *International Journal of Heat*

and Fluid Flow, **25**(3), pp. 393 – 403. Turbulence and Shear Flow Phenomena (TSFP-3).

[5] Sewall, E. A., Tafti, D. K., Graham, A. B., and Thole, K. A., 2006. "Experimental validation of large eddy simulations of flow and heat transfer in a stationary ribbed duct". *International Journal of Heat and Fluid Flow,* **27**(2), pp. 243 – 258.

[6] Wang, L., Hejcik, J., and Sunden, B., 2007. "Piv measurement of separated flow in a square channel with streamwise periodic ribs on one wall". *Journal of Fluids Engineering,* **129**(7), pp. 834–841.

[7] Wang, L., Salewski, M., and Sundén, B., 2008. "Identification and analysis of vortical structures in a ribbbed channel". In Proceedings of ASME 2008 Summer Heat Transfer Conference, American Society of Mechanical Engineers (ASME). Paper number FEDSM2008-55055.

[8] Wang, L., Salewski, M., and Sundén, B., 2010. "Turbulent flow in a ribbed channel: Flow structures in the vicinity of a rib". *Experimental Thermal and Fluid Science,* **34**(2), pp. 165 – 176.

[9] Webb, R. L., 1994. *Principles of Enhanced Heat Transfer*. John Wiley & Sons Inc, New York.

[10] Han, J. C., Glicksman, L. R., and Rohsenow, W. M., 1978. "An investigation of heat transfer and friction for rib-roughened surfaces". *International Journal of Heat and Mass Transfer,* **21**(8), pp. 1143 – 1156.

[11] Lockett, J. F., and Collins, M. W., 1990. "Holographic interferometry applied to rib-roughness heat transfer in turbulent flow". *International Journal of Heat and Mass Transfer,* **33**(11), pp. 2439 – 2449.

[12] Liou, T.-M., and Hwang, J.-J., 1993. "Effect of ridge shapes on turbulent heat transfer and friction in a rectangular channel". *International Journal of Heat and Mass Transfer,* **36**(4), pp. 931–940.

[13] Chandra, P. R., Fontenot, M. L., and Han, J. C., 1998. "Effect of rib profiles on turbulent channel flow heat transfer". *Journal of Thermophysics and Heat Transfer,* **12**(1), pp. 116–118.

[14] Ahn, S. W., 2001. "The effects of roughness types on friction factors and heat transfer in roughened rectangular duct". *International Communications in Heat and Mass Transfer,* **28**(7), pp. 933–942.

[15] Wang, L., and Sunden, B., 2007. "Experimental investigation of local heat transfer in a square duct with various-shaped ribs". *Heat and Mass Transfer,* **43**(8), pp. 759–766.

[16] Hwang, J. J., and Liou, T. M., 1995. "Heat transfer in a rectangular channel with perforated turbulence promoters using holographic interferometry measurement". *International Journal of Heat and Mass Transfer.,* **38**, pp. 3197–3207.

[17] Buchlin, J. M., 2002. "Convective heat transfer in a channel with perforated ribs". *Int. J. Thermal Sci.,* **41**, pp. 332–340.

[18] Panigrahi, P. K., Schröder, A., and Kompenhans, J., 2006. "PIV investigation of flow behind surface mounted permeable ribs". *Experiments in Fluids,* **40**, pp. 277–300.

[19] Panigrahi, P. K., Schröder, A., and Kompenhans, J., 2008. "Turbulent structures and budgets behind permeable ribs". *Experimental Thermal and Fluid Science,* **32**(4), pp. 1011–1033.

[20] Yang, Y.-T., and Hwang, C.-W., 2004. "Numerical calculations of heat transfer and friction characteristics in rectangular ducts with slit and solid ribs mounted on one wall". *Numerical Heat Transfer Part A: Applications,* **45**, pp. 363–375(13).

[21] Kukreja, R. T., and Lau, S. C., 1998. "Distributions of local heat transfer coefficient on surfaces with solid and perforated ribs". *Journal of Enhanced Heat Transfer,* **5**(1), pp. 9–21.

[22] Salewski, M., Stankovic, D., and Fuchs, L., 2008. "Mixing in Circular and Non-Circular Jets in Crossflow". *Flow, Turbulence and Combustion,* **80**, pp. 255–283.

[23] Cui, J., Patel, V. C., and Lin, C. L., 2003. "Large-eddy simulation of turbulent flow in a channel with rib roughness". *International Journal of Heat and Fluid Flow,* **24**, pp. 372–388.

[24] Adrian, R. J., Christensen, K. T., and Liu, Z. C., 2000. "Analysis and interpretation of instantaneous turbulent velocity fields". *Experiments in Fluids,* **29**, pp. 275–290.

[25] Duwig, C., Salewski, M., and Fuchs, L., 2008. "Simulations of a Turbulent Flow Past a Sudden Expansion: A Sensitivity Analysis". *AIAA Journal,* **46**(2), pp. 408–419.